Available online at www.sciencedirect.com
SCIENCE DIRECT®
Acta Materialia 53 (2005) 1153–1165
Acta MATERIALIA
www.actamat-journals.com

Role of particle size and filler–matrix adhesion on dynamic fracture of glass-filled epoxy. I. Macromeasurements

R. Kitey, H.V. Tippur *

Department of Mechanical Engineering, 202 Ross Hall, Auburn University, Alabama 36849, USA

Received 30 April 2004; received in revised form 4 November 2004; accepted 5 November 2004
Available online 10 December 2004

Abstract

The roles of particle size and filler–matrix adhesion strength in the dynamic fracture behavior of glass-filled epoxy are studied. Spherical particles of size 7–200 μm are used to reinforce epoxy matrix at a constant volume fraction (10%) and two different filler–matrix strengths, weak and strong. Optical interferometry in conjunction with high-speed photography has provided information regarding instantaneous crack tip positions and deformations when samples are subjected to impact loading. The crack velocity and stress intensity factor histories are extracted from the interferograms. Elastic characteristics remain unaffected by neither the particle size nor filler–matrix adhesion. Both weakly and strongly bonded particles in the matrix show higher values of fracture toughness relative to unfilled matrix material. Filler particle size affects fracture toughness significantly when the particles are used in the uncoated (or, weakly bonded) state. Additionally, a particle size of 35 μm is seen to enhance the fracture toughness the most when compared to both smaller and larger size uncoated particles. An inverse relationship seems to exist between steady state fracture toughness and crack velocity for different particle sizes. Unlike weakly bonded filler particles, the size effect essentially vanishes when the filler–matrix adhesion is enhanced using silane treatment.

Keywords: Particulate composites; Matrix reinforcement; Optical measurements; Impact loading; Dynamic fracture

1. Introduction

Polymeric particulate composites are widely used in engineering applications due to their many desirable thermo-mechanical properties as well as relatively low manufacturing cost. The macroscopic isotropy of these composites is also quite attractive for mechanical design. The addition of rigid filler particles to the polymer matrix generally increases the overall stiffness of the mixture. The accompanying reduction in the coefficient of thermal expansion and the improvement in creep resistance are other favorable aspects. The properties of the constituent phases (filler and matrix), filler volume fraction, filler particle size and shape, and filler–matrix interfacial strength significantly influence these overall properties in general and failure properties such as tensile strength and fracture toughness of particulate composites. Previous attempts on quantifying these have generally been made under quasi-static loading conditions and dynamic responses are largely unknown at the moment. Some of the reported results are reviewed briefly in the following.

Spanoudakis and Young [1,2] have shown that the critical stress intensity factor K_{Ic} decreases with an increase in particle size at lower volume fractions, while critical energy release rate G_{Ic} drops with increasing particle size to a minimum value at 47 μm particle diameter. They have suggested that the toughening mechanism is due to the crack front pinning followed by crack tip blunting due to the break down of particle–matrix inter-

* Corresponding author. Tel.: +1 334 844 3327; fax: +1 334 844 3307.
E-mail address: htippur@eng.auburn.edu (H.V. Tippur).

1359-6454/$30.00
doi:10.1016/j.actamat.2004.11.012

face. They have also concluded that the values of K_{Ic} are not strongly dependent on the strength of adhesion but poor bonding causes an increase in energy release rate due to the reduction of Young's modulus, while filler–matrix interface strength does have strongly favorable effects on fracture strength. The associated mechanism for particle size effect on crack propagation remains to be studied.

Similar results have been reported by Moloney et al. [3], who have investigated 40% volume fraction silica-filled epoxy with particle size in the range of 60–300 μm. Negligible effect of particle size is observed on flexural modulus and fracture toughness, but flexural strength is found to decrease with increasing particle size. Strongly bonded fillers show higher flexural and tensile strengths since weakly bonded particles act as sources of inherent flaws provoking crack initiation. Furthermore they have also observed that weaker matrix–filler interface results in higher fracture toughness due to possible crack tip blunting.

Nakamura et al. [4] have investigated particle size and particle–matrix adhesion effects on flexural and fracture properties for 35% volume fraction for 2–30 μm spherical silica-filled epoxy. Increase in flexural strength with decreasing particle size has been noticed. The effect is more prominent for strongly bonded silica particles, while there is only a slight increase in flexural modulus with increase in particle size and with no dependence on adhesion strength. On the contrary, prominent increase in K_{Ic} with increase in particle size has been noticed due to increased crack deflection, interfacial debonding and particle fracture. They have also noticed that there is no effect of bonding strength for K_{Ic}. In a similar investigation [5] on silica-filled epoxy with particle size range of 2–42 μm (55% and 64% weight fraction), both fracture toughness and energy release rate is reported to have increased with increase in particle size. Static fracture tests based on 3-point bend specimens show higher toughness when compared to double torsion and impact fracture tests.

Second phase inhomogeneities dispersed in a brittle matrix act as obstacles impeding the moving crack front thereby increasing fracture toughness either by increasing the length of the crack front and/or by blunting the crack tip. Crack deflection, bowing, and crack tip blunting are very common phenomena in the presence of second phase material in the vicinity of a propagating crack front causing reduction in stress intensity. The toughening mechanism depends on the characteristics of the constituent phases, crack front interaction, and the filler–matrix bonding strength. Various models have been proposed to predict crack path perturbation in the presence of second phase material and the crack tip blunting mechanism in case of failure of filler–matrix bonding.

Analogous to dislocation pinning, Lange [6] has proposed a widely cited theory about line tension, according to which the propagating crack front bows out between dispersed impenetrable second phase particles while remaining pinned at the locations where it interacts with the particles. This increases the length of the crack front depending upon inter-particle spacing. As a result the total energy for fracture increases by an amount required to increase the length of the crack front rather than just the energy needed to form new surfaces as in case of unfilled materials. The functional relation between fracture energy of a composite material G_{Ic} and the average spacing between second phase particles l is given by

$$G_{Ic} = 2\left(\gamma_0 + \frac{T}{l}\right), \tag{1}$$

where γ_0 is surface energy per unit area and T is line energy per unit length of the crack front. The relation clearly indicates that fracture resistance of a composite increases as the distance between the dispersed second phase particles decreases. Further Evans [7] has demonstrated by calculating T for various configurations of bowed out crack front between the particles that line energy to fracture energy ratio is a function of both particle size and spacing. And the major contribution to the increase in strength is from crack extension stress, which is larger than the stress needed to propagate an unbowed crack, dependent on the ratio of particle dimension to the inter-particle spacing.

Faber and Evans [8,9] have proposed models to predict the increase in fracture toughness due to crack deflection around secondary phase material by determining initial tilt and maximum twist of the crack front between the particles causing lower crack driving force, and consequently increased fracture toughness. The tilt angle depends on the orientation and the position of the particle with respect to an advancing crack front and the presence of residual stresses developed between filler and matrix, causing reduction in stress intensity in mode I and mode II. The magnitude of crack twist depends upon the orientation of adjacent particles forcing the crack to tilt in opposite directions resulting in mode I and mode III. Both the models and experimental results conclude that there is a dependence of fracture toughness on the shape and the volume fraction of second phase material while being invariant of particle size. Ahmed and Jones [10] have reviewed various theoretical models showing the effects of particle size, filler–matrix adhesion strength and volume fraction on elastic modulus and tensile strength.

As can be seen from the above review of the literature, most of the studies have been performed for static loading conditions and very limited literature is available on particle size and filler–matrix interface strength effect under dynamic loading conditions. Also, it should be

noted that none of the available dynamic results provide complete pre- and post-crack initiation behaviors. Further, conclusions drawn contain significant differences among the investigations. While some have reported an increase in K_{Ic} as particle size decreases, others report either a decreasing trend or no effect at all. Similar differences can be noticed in case of filler–matrix adhesion effect when some investigators have noticed no effect on K_{Ic} while others have reported decreasing K_{Ic} with increasing filler–matrix adhesion strength.

In this paper particle size and filler–matrix adhesion effect on fracture behavior of glass-filled epoxy have been investigated under impact loading conditions. Solid glass spheres of various sizes in the range of 7–200 μm in diameter for both weak and strong filler–matrix interfacial strength have been studied. Crack initiation and crack growth phenomena along with crack tip deformations have been measured using high-speed imaging and optical interferometry. These measurements have been used to determine macroscopic fracture parameters.

2. Material preparation and characterization

The role of particle size and filler–matrix adhesion strength in dynamic fracture behavior are quite evident even at relatively low volume fractions. Hence 10% volume fraction (V_f) of soda-lime glass (A-glass) spheres of bulk density 2500 kg/m^3 was chosen to prepare glass-filled epoxy specimens throughout this study. The low V_f could also assist in avoiding agglomeration problems, especially for smaller particles. Solid glass spheres of mean diameters 7, 11, 35, 71 and 203 μm were used to study particle size effect. To study filler–matrix adhesion effect, weak and strong filler–matrix interfaces were created by using uncoated and silane coated particles of the above mentioned sizes. It should be noted that particle sizes 11, 35 and 203 μm are the only ones available commercially for the silane treated case. Low viscosity epoxy, prepared by mixing bisphenol-A resin and amine-based hardener of densities 1129.9 and 961.2 kg/m^3 in the ratio of 100:36, was used as matrix material. Epoxy and spherical glass particles were mixed for 30 min before being poured into a mold. The material was cured at room temperature for approximately 72 h.

Physical and elastic properties of uncoated and silane coated composites are tabulated in Tables 1 and 2. Longitudinal and shear wave speeds (C_l and C_s) were measured by pulse-echo method at discrete locations of the cured material. Transit time for the pulse to travel twice the thickness of the sample was measured with the help of a digital oscilloscope (Gould model 5052*UA*) and longitudinal wave transducer (Panametrics #V129RM; 10 MHz) and shear wave transducer (Panametrics #V156RM; 5 MHz). Dynamic elastic Modulus E_d and Poisson's ratio ν_d are calculated using,

$$C_l = \sqrt{\frac{E_d(1-\nu_d)}{\rho(1+\nu_d)(1-2\nu_d)}}, \qquad C_s = \sqrt{\frac{E_d}{2\rho(1+\nu_d)}}, \tag{2}$$

where ρ is the mass density of the composite.

Cast sheets were machined into test samples of dimensions 152 mm × 42 mm × 8 mm. The surface was then roughened with 150 grit size sand paper. Subsequently, the surface was made optically flat and specular by transferring a thin (a few nm thick) aluminum film using an optical flat and a layer of epoxy. An edge notch of root radius 150 μm and nominal length of 10 mm was

Table 1
Material properties of (uncoated) weakly bonded glass-filled epoxy, $V_f - 0.1$

Average particle diameter D (μm)	Density ρ (kg/m^3)	Longitudinal wave speed C_l (m/s)	Shear wave speed C_s (m/s)	Elastic modulus E_d (GPa)	Poisson's ratio ν_d
203	1279	2567	1174	4.83	0.368
71	1282	2585	1182	4.90	0.368
35	1296	2550	1172	4.87	0.366
11	1291	2561	1188	4.97	0.363
7	1298	2581	1183	4.97	0.367
Epoxy	1132	2468	1109	3.82	0.374

Table 2
Material properties of (silane coated) strongly bonded glass-filled epoxy, $V_f - 0.1$

Average particle diameter D (μm)	Density ρ (kg/m^3)	Longitudinal wave speed C_l (m/s)	Shear wave speed C_s (m/s)	Elastic modulus E_d (GPa)	Poisson's ratio ν_d
203	1286	2536	1181	4.89	0.361
35	1285	2535	1172	4.82	0.364
11	1278	2577	1190	4.94	0.365

cut into the sample using a high-speed diamond impregnated circular saw.

3. Macromeasurements

3.1. Experimental details

The optical method of coherent gradient sensing (CGS) [11–13] has been used to study crack tip deformations in particle filled composite specimens. CGS measures in-plane gradients of out-of-plane surface displacements (surface slopes) around a crack tip when used to study opaque solids. The relative ease of implementation of CGS when used in conjunction with high-speed cameras is attractive for the study dynamic crack growth problems.

The schematic of experimental set-up for reflection CGS is shown in Fig. 1. A collimated beam of coherent laser light illuminates an opaque specimen with a specularly reflective surface. The reflected object wave front is incident on a pair of high-density Ronchi gratings G_1 and G_2, spatially separated by a distance Δ, as shown. These parallel gratings diffract the object wave-front successively in several discrete directions. The filtering lens L collects the field distribution and displays its frequency content on its back focal plane as a series of diffraction spots as shown. By locating the filtering aperture around ± 1 diffraction order, the information about surface slopes in the form of interference fringes is captured at the image plane. The optical set-up requires that the imaging system be focused on the object surface.

The experimental set-up includes an impactor, a pulse laser, CGS interferometer and a continuous access high-speed camera. An argon-ion laser beam (wave length $\lambda = 514$ nm) is expanded and collimated into a 50 mm diameter beam. A pneumatically operated cylindrical steel hammer with hemispherical tip is used to impact (velocity 5.3 m/s) the center of the specimen along the negative x-axis, as shown in the schematic. The specimen was initially rested on two soft-putty blocks to simulate free–free supports. Before the impactor hits the specimen, a flag (of width $\sim$6.4 mm) triggers a photodetector which in turn opens a "capping shutter" in front of the camera. This allows laser beam to expose a strip of T-MAX400 photographic film located in a circular track in the camera. As soon as the impactor touches an adhesive backed copper tape on the top edge of the specimen, an electric circuit initiates a gate pulse of 320 μs duration. Laser pulses of 50 ns width are repeated at 5 μs intervals (200,000 fps) during the gate period. With these settings, approximately 70 images are exposed onto the photographic film. The incident beam upon reflecting from the deformed surface carries the information about the non-planarity of the surface near the crack tip and the impact point. The angular deflections of light rays relative to the optical axis are measured as interference fringes by filtering out all but ± 1 diffraction order. The fringe patterns representing contours of $\partial w/\partial x$ are recorded in this study.

Interference fringes are the outcome of stress waves generated by the impact that travel back and forth across the sample, loading the notch tip to initiation. A crack subsequently propagates dynamically, at speeds of up

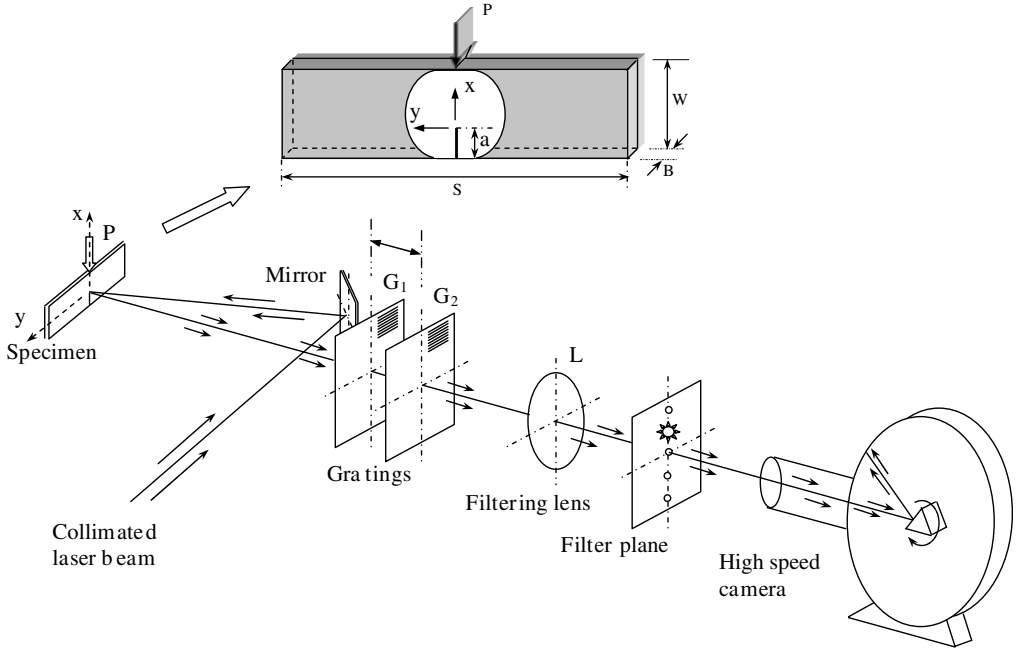

Fig. 1. Experimental set-up (specimen dimensions are $S = 152$ mm, $W = 42$ mm, $B = 8$ mm, $a = 10$ mm).

to 530 m/s in some specimens. Highly discernible fringes on the specimen surface around the impact point and crack tip are evident from the representative interferograms shown in Fig. 2. The first set of four fringes in Fig. 2(a) are for 11 μm weakly bonded particles, next four (Fig. 2(b)) for 35 μm and third set in Fig. 2(c) is for 203 μm particles, all for weakly bonded fillers in the matrix. In each set, the first two images are for pre-crack initiation instants while the next two are from post-initiation time instants. Impact point fringes (at the top of every image) develop and start accumulating as soon as the impactor contacts the specimen, while the crack tip fringes start appearing after about 35–40 μs after the initial impact. As the stress waves reach the crack tip, trilobed fringes symmetric about the crack representing mode-I deformations start evolving around the crack tip. Second image in each set is a fringe pattern just before crack initiation. At initiation, sudden release of energy results in stress waves emanating from the crack tip seen as a circular discontinuity in an otherwise continuous fringe pattern centered at the initial notch tip (third image of each set). After initiation, nearly stable crack growth ensues for about 40–60 μs. This is followed by a monotonic reduction in the size of lobes. These fringes represent contours of $\partial w/\partial x$ where w is out-of-plane displacement. The resolution of the fringes is ≈0.015°/fringe.

3.2. Fringe analysis

Surface deformations are measured in terms of fringe order N, grating pitch p and grating separation distance Δ. In the present work, the principal direction of the gratings is chosen to be along x-axis. Accordingly, the governing equation [11] can be written as,

$$\frac{\partial w}{\partial x} = \frac{Np}{2\Delta} \quad N = 0, \pm 1, \pm 2, \pm 3, \ldots, \tag{3}$$

which can be expressed in terms of stress gradients for plane stress conditions as

$$\frac{\partial w}{\partial x} \approx -\frac{\nu B}{2E}\left[\frac{\partial(\sigma_x + \sigma_y)}{\partial x}\right] = \frac{Np}{2\Delta}, \tag{4}$$

where E is the elastic modulus, ν is the Poisson's ratio and B is the undeformed thickness of the specimen. Considering linear elastic asymptotic stress field in the vicinity of a steadily propagating mode-I crack [13],

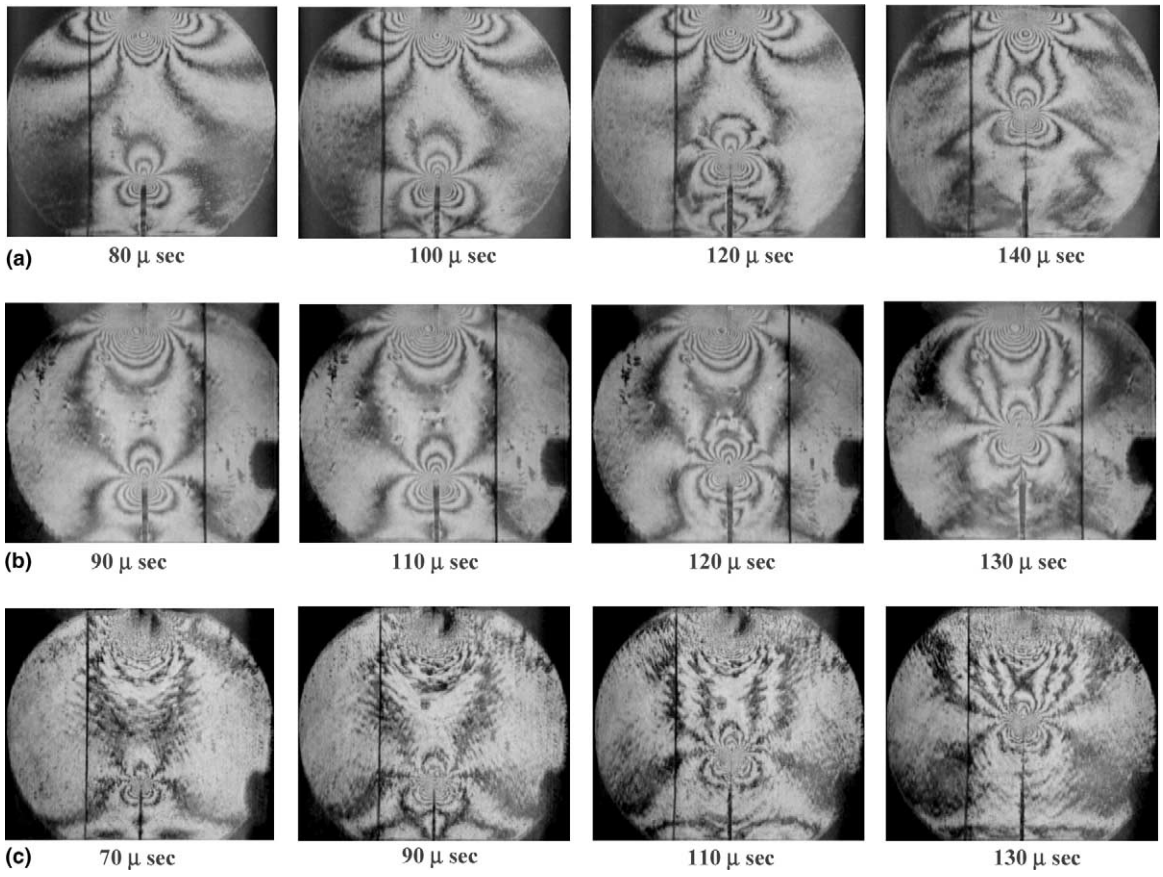

Fig. 2. Selected fringe pattern representing surface slope contours of $\partial w/\partial x$ for weakly bonded glass-filled epoxy specimens, (a) 11 μm particles, (b) 35 μm particles, (c) 203 μm particles. Indicated time corresponds to the instant after impact.

$$\frac{\partial w}{\partial x} = -\frac{vB}{2E} f(v) \sum_{n=1}^{\infty} \left[A_n \left(\frac{n}{2} - 1\right) r_1^{\left(\frac{n}{2}-2\right)} \cos\left(\frac{n}{2} - 2\right)\theta_1 \right] = \frac{Np}{2\Delta}, \quad (5)$$

where

$$f(v) = \frac{(1+\alpha_s^2)(\alpha_l^2 - \alpha_s^2)}{4\alpha_l\alpha_s - (1+\alpha_s^2)^2},$$

$$\theta_l = \tan^{-1}(\alpha_l \tan\theta),$$

$$r_l = r\cos\theta(1 + \alpha_l \tan^2\theta),$$

$$\alpha_{l:s} = \sqrt{1 - (v/C_{l:s})^2}, \quad (6)$$

r and θ are the polar coordinates defined at the instantaneous crack tip. Eq. (5) can also be used for analyzing pre-initiation interferograms as $f(v) \to 1$ as $v \to 0$, reducing the equation to the form of its quasi-static counterpart. Overdeterministic least-squares analysis is performed on Eq. (5) and the resulting functional is minimized with respect to constants A_n. This results in a set of linear equations of the form,

$$[Q]\{A\} = \{Z\}. \quad (7)$$

In Eq. (7), $\{A\}$ is the vector of unknown constants A_n with $A_1 = K_I\sqrt{2/\pi}$, $[Q]$ is the matrix with its elements $Q_{ij} \equiv Q_{ij}(r, \theta, v, C_l, C_s)$ and $\{Z\}$ is known vector of $Z_i \equiv -Z_i(r, \theta, N, E, \nu, B, v, C_l, C_s)$. The resulting set of linear equations can be solved to get A_n.

3.3. Crack velocity and stress intensity factor

The framing rate of the high-speed imaging system is set to capture the images once every 5 μs after impact. Instantaneous crack length is measured by locating the crack tip from digitized images. From crack tip location histories, crack velocities are calculated using central difference method:

$$v_i = \left(\frac{da}{dt}\right)_i = \frac{a_{i+1} - a_{i-1}}{t_{i+1} - t_{i-1}}. \quad (8)$$

Interferograms are used to extract fracture parameters by digitizing optical information around the crack tip to obtain fringe location, (r, θ), and fringe order, N, data. Using the least-squares analysis described previously, mode-I dynamic stress intensity factors K_I are evaluated. The region of dominant 3-D effects in the vicinity of the crack tip ($r/B < 0.5$) is excluded from the analysis. Also, only the data behind the crack ($90° < \theta < 150°$) is considered since it has been demonstrated that triaxial effects are at a minimum in this region [11]. Since the measured data considered in the analysis comes from a region beyond $r/B = 0.5$, the inclusion of non-singular terms in the least-squares analysis is needed to account for far-field stresses. It has been found that by including first three terms of asymptotic stress field, K_I can be evaluated accurately.

4. Results and discussion

4.1. Experimental repeatability

Fig. 3(a) shows crack growth histories in two specimens with 35 μm uncoated particles. Both sets of data show crack initiation at 105 μs with an experimental accuracy of 5 μs. The instantaneous increase in velocities up to about 400 m/s can be noticed initially. The instantaneous release of energy from the initial notch results in rapid acceleration to about 4×10^7 m/s^2 and a maximum velocity (v_{max}) of about 30% of Rayleigh wave speed following crack initiation. The history shows a drop in velocity following this initial acceleration to a steady state value (v_{ss}) of approximately 300 m/s. The steady state crack growth region is followed by a continuous drop in velocity as the free surface and impact points

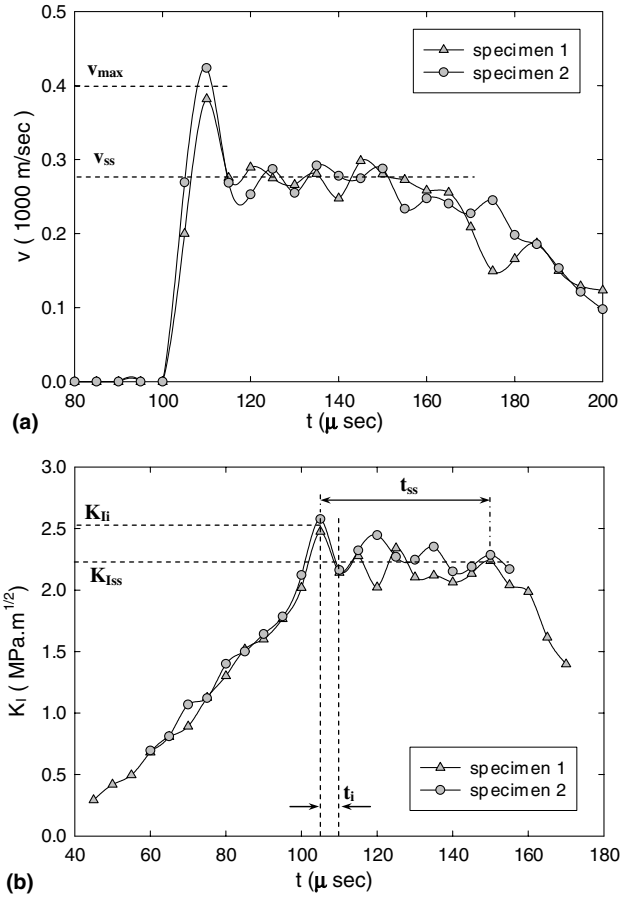

Fig. 3. Crack velocity histories (a) and stress intensity factor histories (b) for two identical specimens with 35 μm uncoated filler particles demonstrating repeatability of experimental measurements.

are encountered by the propagating crack tip. The fracture is complete at ~260 μs in both the specimens.

The stress intensity factor histories for the same two specimens with 35 μm uncoated filler particles are shown in Fig. 3(b). In each case the stress intensity factor increases monotonically up to crack initiation. Pre-initiation stress intensity factor histories for both specimens essentially coincide. The rate of increase of stress intensity factor until crack initiation is $\sim 34 \times 10^3$ MPa $\sqrt{\text{m}}$/s. In both of the experiments the crack initiated at ~105 μs and crack initiation toughness was $K_{\text{Ii}} \sim 2.5$ MPa $\sqrt{\text{m}}$. Crack initiation is associated with a sudden drop in stress intensity factor which can be noticed in the figure. The maximum value of K_{I} just before the drop is identified as K_{Ii}. Further, instantaneous values of post-crack initiation stress intensity factors show oscillatory behavior due to discrete wave reflections driving the crack forward. Oscillations can also be attributed to microstructural inhomogeneities. (It should be noted that such oscillations occur even in monolithic materials such as unfilled epoxy, which is discussed later.) Intermittent interactions of a propagating crack front with particles and particle clusters give rise to different amounts of crack-tip shielding [14,15] and failure mechanisms [8]. These in turn affect crack velocity histories as well as stress intensity factor histories. The post crack initiation oscillations continue for about 50 μs. The average value of stress intensity factor for the period is identified as steady state fracture toughness K_{Iss} of the material. For both the specimens post-crack initiation steady state fracture behaviors are nearly similar, with a K_{Iss} of ~2.35 MPa $\sqrt{\text{m}}$. The steady state behavior is followed by a monotonic drop in K_{I} until the specimen fracture is complete. The accuracy of fringe analysis beyond 160 μs is relatively low due to severe interaction between crack tip and impact point deformation fields.

Similarity of pre- and post-initiation behavior for crack tip velocity and stress intensity factor histories in multiple specimens suggest the robustness and repeatability of the experiments and the method employed in this study. Similar repeatability tests have also been undertaken successfully for several other particle sizes and interfacial strengths.

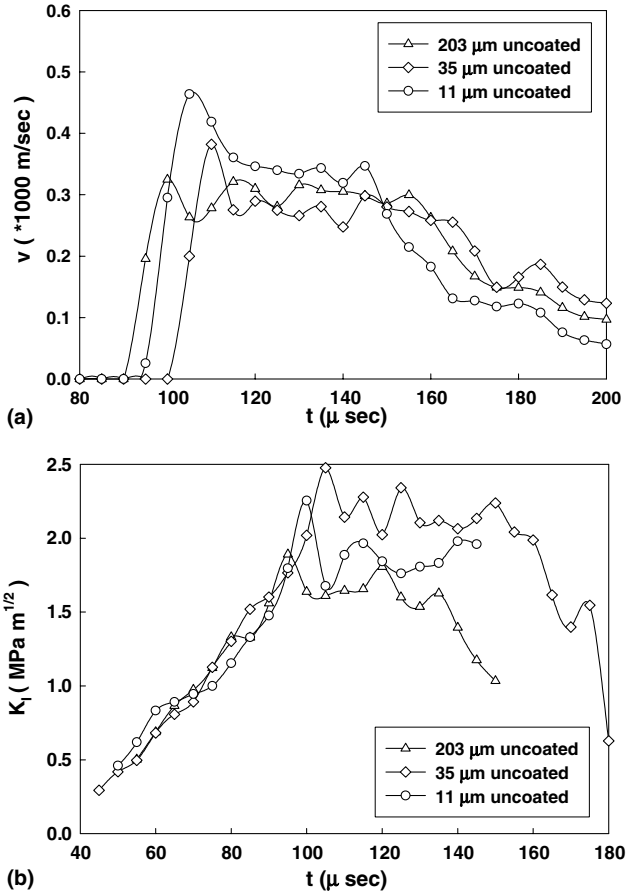

Fig. 4. Crack velocity histories (a) and Stress intensity factor histories (b) for different glass-filled epoxy specimens with weakly bonded (uncoated) particles.

4.2. Particle size effect

4.2.1. Weakly bonded (uncoated) particles

Crack velocity histories for specimens with weakly bonded fillers are shown in Fig. 4(a). Only the results for 11, 35 and 203 μm sizes are shown in order to avoid data clutter and consistent comparison with strongly bonded fillers to be presented in the next section. In each case crack velocity history shows a rapid increase in velocity at crack initiation reaching a maximum value $v_{\max}$, followed by a noticeable drop. Subsequently, crack

Table 3
Crack growth parameters for glass-filled epoxy with weakly bonded filler ($V_{\text{f}} = 0.1$)

Particle diameter D (μm)	Crack initiation time t_{i} (μs)	Maximum crack velocity $v_{\max}$ (m/s)	Steady state crack velocity v_{ss} (m/s)	Steady state duration t_{ss} (μs)	Crack initiation toughness K_{Ii} (MPa $\sqrt{\text{m}}$)	Steady state fracture toughness K_{Iss} (MPa $\sqrt{\text{m}}$)
203	95–100	325	310	55	1.89	1.67
71	100–105	341	300	50	2.19	1.92
35	105–110	382	285	45	2.48	2.31
11	100–105	464	345	35	2.25	1.96
7	110–115	493	370	25	1.97	1.87
epoxy	125–130	350	325	45	2.28	1.5

velocity is oscillatory about an average value identified as steady state velocity, v_{ss}. Some of these observations about crack initiation and growth are quantified in Table 3. The maximum crack velocity and acceleration at crack initiation increases as the particle size decreases. In the current study the maximum velocity ranges between ~325 m/s for the largest particles to ~500 m/s for the smallest. The acceleration at crack initiation is of the order of 10^7 m/s^2. As the particle size decreases, duration of steady state crack growth, t_{ss}, decreases. That is t_{ss} is the least for the smallest particle size and longest for the largest particle size. It is noticed in these experiments that specimen fracture is complete at nearly the same time, ~260 μs, irrespective of the particle size. As the particle size decreases, maximum velocities increase. Since all the specimens take the same time to fail completely, the duration of steady state growth t_{ss} decreases for smaller particles at the cost of higher maximum velocities. Table 3 shows minimum steady state velocity in case of 35 μm particles. Further increase or decrease in particle size only results in an increase in steady state velocity. This interesting velocity trend, which can be related to steady state fracture toughness, will be discussed later on.

Stress intensity factor histories for specimens with weakly bonded particles (same particle sizes as in Fig. 4(a), for consistency) of various particle sizes are shown in Fig. 4(b). For each particle size, stress intensity factors monotonically increase until crack initiation. The average rate of increase in each case is $\sim 32 \pm 3$ MPa$\sqrt{\text{m}}$/ms. The similarity of pre-initiation stress intensity factor histories suggest nearly same crack tip loading rate. This in turn can be attributed to similar macroscopic elastic wave characteristics (Table 1) irrespective of particle size and filler–matrix adhesion strength. Crack initiation time varies from 95 to 115 μs for the considered particle sizes. In each case, crack initiation is followed by a small drop in K_I value followed by a sustained oscillatory behavior about an average. Notations K_{Ii} and K_{Iss} will henceforth be used for maximum and steady state fracture toughness values, respectively. The K_{Ii} and K_{Iss} values for all weakly bonded particles are also tabulated in Table 3. The steady state fracture toughness of unfilled epoxy ($\approx 1.5 \pm 0.1$ MPa$\sqrt{\text{m}}$) is considered as a reference for further comparisons (see Fig. 5 [1] and Table 3). Specimens with 35 μm particles show the highest value of K_{Iss}, which is approximately 65% higher when compared to the one for unfilled epoxy. With a decrease or an increase in particle sizes relative to 35 μm size, K_{Iss} shows decreasing trend. Specimens with 11 μm particles show 40% and 7 μm particles show 34% higher fracture toughness, respectively, compared to the unfilled epoxy. From Table 3 it can be noticed that both 11 and 7 μm show similar stress intensity factor behaviors, with a relatively small difference in K_{Iss} suggesting possible saturation of fracture toughness as particle size decreases. Similar effects have been noticed when particle size is increased beyond 35 μm. Specimens with 71 and 203 μm particles show approximately 37% and 18% increase in fracture toughness compared to unfilled epoxy, which is successively lower compared to the ones with 35 μm particles. Fig. 6 summarizes particle size effect on K_{Iss} in case of weakly bonded filler at 10% volume fraction. Evidently, there is a discernible optimum particle size at which fracture toughness is maximum for the selected volume fraction. As the particle size increases or decreases relative to this optimum value, steady state fracture toughness decreases. Quite interestingly the optimum particle size for maximum steady state fracture toughness also corresponds to the minimum steady state velocity. With a decrease or an increase in particle size relative to the

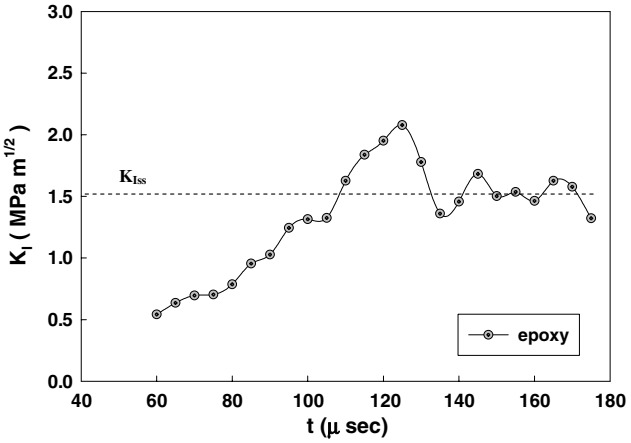

Fig. 5. Stress intensity factor history for unfilled epoxy.

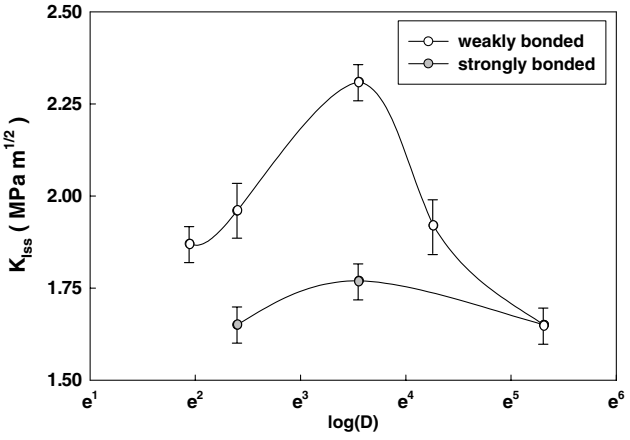

Fig. 6. Particle size effect on steady state fracture toughness.

[1] Stress intensity factor history for unfilled epoxy is shown in Fig. 5 for completeness. The overall features here are similar to the ones shown for glass-filled specimens. That is, a monotonic increase ($\partial K_I/\partial t \sim 25$ MPa$\sqrt{\text{m}}$/ms) in K_I up to initiation is followed by a drop and a steady state value at around ~1.5 MPa$\sqrt{\text{m}}$ can be seen.

optimum value, monotonic decrease in fracture toughness is associated with increase in steady state velocity. That is, an inverse relationship between steady state velocity and fracture toughness seems to exist. From Table 3 it can also be noticed that K_{Ii} trends are similar to that of K_{Iss}. The trends again show optimum particle size to be 35 μm. Comparison shows that K_{Ii} is higher by 35%, 56%, 77%, 61% and 41% for 203, 71, 35, 11 and 7 μm, respectively, compared to the unfilled epoxy. Similarly a decreasing trend in fracture toughness for particle sizes below 35 μm has been reported by Nakamura et al. [4,5], who have studied the particle size effect in silica-filled epoxy of 2–42 μm particle range.

4.2.2. Strongly bonded (silane treated) particles

To study the particle size effect on fracture behavior in the case of silane treated filler, experiments have been performed on three particle sizes, 203, 35 and 11 μm. The selection of particle sizes here is limited due to the commercial availability. Figs. 7(a) and (b) show crack velocity and stress intensity factor histories. For each particle size, crack velocity variations show rapid increase at initiation, with an estimated acceleration of the order of $\sim 10^7$ m/s^2, for all three particle sizes. As in case of uncoated particles, maximum velocity (v_{max}) is followed by a noticeable drop and a steadily oscillatory behavior with an average value denoted by v_{ss}. From Table 4 it can be noticed that both v_{max} and v_{ss} increase as particle size decreases. The duration of steady state crack growth t_{ss} decreases with the increase in steady state velocity and hence with the decrease in particle size. Further, the steady state crack growth region is followed by monotonic drop in crack velocity until complete fracture.

Similar to weakly bonded particles, stress intensity factor histories in Fig. 7(b) show monotonic increase in K_I until crack initiation for all particle sizes, with an average crack tip loading rate of 30 ± 3 MPa $\sqrt{m}$/ms. As before, crack initiation is followed by a small drop in K_I and a steadily oscillating value identified by K_{Iss}. Unlike weakly bonded particles, strongly bonded particles do not show significant variation in K_{Iss} as particle size is varied. From stress intensity factor histories in Fig. 7(b) and Table 4 it is quite clear that steady state fracture toughness values for various particle sizes are rather close to each other, suggesting only a marginal effect of particle size on fracture toughness in the case of strongly bonded particles. Specimens with 35 μm particles still show slightly higher fracture toughness when compared to the other two particle sizes. Since silane treatment increases filler–matrix interface strength, one can conjecture that for ideal filler–matrix interface strength, particle size effect on fracture toughness would potentially vanish.

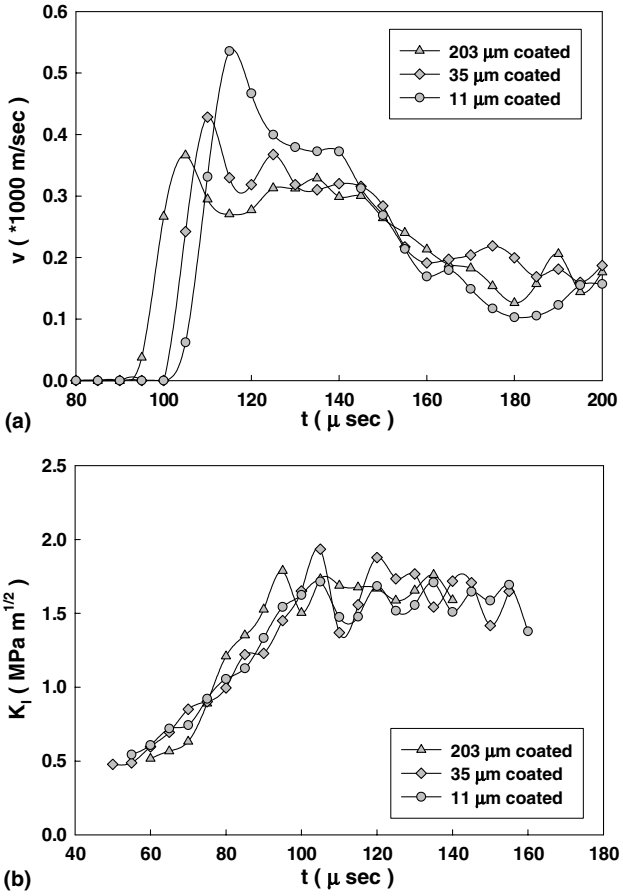

Fig. 7. Crack velocity history (a) and Stress intensity factor history (b) in glass-filled epoxy specimens with strongly bonded (silane treated) particles.

4.3. Filler–matrix adhesion effect

From Tables 3 and 4 and Figs. 4(a) and 7(a) it can be concluded that increasing the filler–matrix interface strength increases the maximum as well as steady state

Table 4
Crack growth parameters for glass-filled epoxy with strongly bonded filler ($V_f = 0.1$)

Particle diameter D (μm)	Crack initiation time t_i (μs)	Maximum crack velocity v_{max} (m/s)	Steady state crack velocity v_{ss} (m/s)	Steady state duration t_{ss} (μs)	Crack initiation toughness K_{Ii} (MPa $\sqrt{m}$)	Steady state fracture toughness K_{Iss} (MPa $\sqrt{m}$)
203	95–100	366	312	35	1.79	1.65
35	105–110	428	320	30	1.93	1.77
11	105–110	536	375	15	1.73	1.65

crack velocities. Specimens with strongly bonded particles show 12–15% (8–10%) higher maximum (steady-state) velocities when compared to the ones with weakly bonded particles for similar particle sizes. As noted earlier for weakly bonded particles, steady state velocity shows an inverse trend with the duration of steady state velocity t_{ss}. For strongly bonded particles steady state velocities are marginally higher and hence there is a smaller steady state duration compared to the case of weakly bonded particles. No discernible filler–matrix adhesion effect can be noticed regarding crack initiation time by comparing t_i for weakly and strongly bonded particles in Tables 3 and 4 for the same particle sizes.

The effect of filler–matrix adhesion on fracture toughness can be quantified from Tables 3 and 4 and Figs. 4(b) and 7(b). Unlike weakly bonded particles, particle size does not affect fracture toughness prominently in the case of strongly bonded filler. This suggests that increasing the filler–matrix adhesion affects the fracture toughness somewhat negatively under dynamic loading conditions, contrary to the conventional wisdom that increasing the filler–matrix bonding strength is generally beneficial. Negative filler–matrix adhesion effect on fracture toughness has also been seen by Moloney et al. [3] who have studied 40% silica filled epoxy in 60–300 μm range.

Fig. 6 summarizes the particle size and filler–matrix adhesion effects. Error bars shown in the figure are based on multiple experiments. A variation of K_{Iss} for strongly bonded fillers is found to be in the range 1.6–1.8 MPa$\sqrt{m}$. This essentially suggests relatively small particle size effect in the case of silane treated fillers. Also K_{Iss} values are consistently higher for uncoated particles even after considering the error bars. This negative filler–matrix adhesion effect decreases as the particle size departs more and more from the optimum value. It should be noted that the experimental error bars are nearly the same for different particle sizes and filler–matrix adhesion.

From Tables 3 and 4 it can be noticed that maximum increase in fracture toughness for weakly bonded filler is for 35 μm particles, which is ~30% higher compared to strongly bonded 35 μm particles. Weakly bonded 11 μm particles show ~18% increase in K_{Iss} values relative to strongly bonded 11 μm particles. Material with 203 μm particles shows negligible effect of filler–matrix adhesion on fracture toughness. Similar trends can be noticed with regard to K_{Ii}, which are 5%, 30% and 30% higher for 203, 35 and 11 μm weakly bonded particles, respectively, as compared to strongly bonded ones.

4.4. Quantitative microscopy

Fig. 6 shows non-monotonic bell-shaped variation of fracture toughness suggesting an optimum particle size among the sizes considered. Although reduction in K_{Iss} for larger particles (>35 μm in this case) is somewhat anticipated, reduction for smaller size particles raise questions about possible agglomeration of particles. Further, consistently lower steady state fracture toughness in case of coated particles when compared to uncoated fillers also raises the possibility of silane induced agglomeration. To investigate these, specimens were sliced and examined using optical microscopy. Samples with cross-sectional area of 25 mm × 8 mm were cut from the specimens studied earlier. The samples were polished using 1000 and 2000 grit wet emery followed by 1 μm diamond paste and 0.04 μm alumina suspension. Representative micrographs shown in Fig. 8(a) are for 35 and 11 μm uncoated and silane coated particle specimens, respectively. Qualitatively, agglomeration is absent in all micrographs, suggesting neither size induced nor silane treatment induced agglomeration. (Dark spots in these micrographs are debris due to polishing.) To confirm the consistency in particle dispersion at different particle sizes (coated and uncoated) three scanned images at random locations of the sample were digitized for each case and quantitative measurements were performed using the *lineal method* [16,17]. Data was collected from 840 μm × 630 μm scanned region for 35 μm particles and 160 μm × 120 μm area for 11 μm particles. A square grid of density $D/8$ was used to calculate volume fraction V_f and inter-particle spacing (volume mean free path) l, where D is the mean particle diameter. The quantities V_f and l were retrieved from digitized images using,

$$V_f = \frac{L_p}{L_t}, \quad l = \frac{1 - V_f}{N_p},$$

where L_p is total transverse intercept length within particle phase and L_t is the total transverse length, as shown schematically in Fig. 8(b). In the above, N_p is the average number of particle hits per unit transverse length. In the calculations, summation of all horizontal and vertical lengths in the grid was taken as the total transverse length. Table 5 shows data on number of particles per unit area, inter-particle separation distance and volume fraction. Similarity in terms of number of particles, volume fraction and inter-particle separation distances, when coated and uncoated cases are compared, suggest that silane coating has not introduced any agglomeration of particles. The same is true even in the case of smaller particle sizes. This strongly suggests that agglomeration of filler particles can be ruled out as the cause of decreasing K_{Iss} at smaller particle sizes (<35 μm) and with silane coating. Further, the average inter-particle separation distance for spherical particles given by Fullman [18],

$$V_f = \frac{2D(1 - V_f)}{3V_f}, \tag{9}$$

closely matches measured inter-particle spacings reported in Table 5.

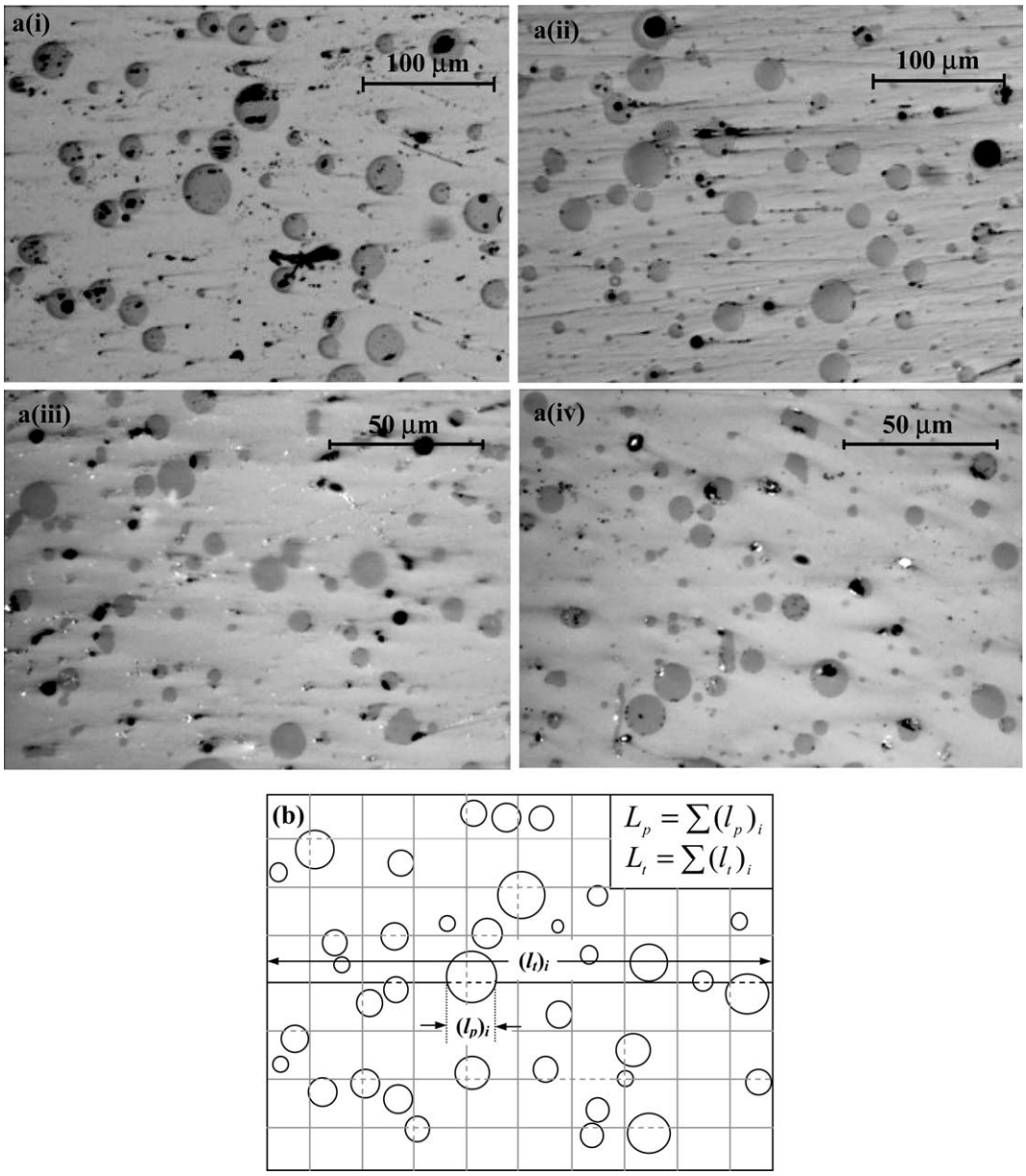

Fig. 8. Optical micrographs of polished surfaces: (a) (i) 35 μm uncoated particles (ii) 35 μm coated particles (iii) 11 μm uncoated particles (iv) 11 μm coated particles, (b) schematic for quantitative analysis of micrographs shown in (a) using lineal method.

Table 5
Quantitative image analysis of polished surface micrographs

Particle diameter (μm)	Average number of particles/area (mm^{-2})	Average inter-particle separation (μm)	Average particle volume fraction
35 (uncoated)	194 ± 4	218 ± 10	10.0 ± 0.1
35 (coated)	192 ± 3	215 ± 12	9.9 ± 0.3
11 (uncoated)	3246 ± 45	56 ± 5	9.7 ± 0.3
11 (coated)	3122 ± 54	59 ± 3	9.5 ± 0.4

4.5. Potential difference in toughening mechanisms

In the literature review a few toughening mechanisms have been mentioned. For silane treated particles where filler–matrix interface is strong, crack deflection mechanism can be presumed to increase the fracture toughness. On the contrary, in uncoated particles filler–matrix interface is weak. This gives rise to crack tip blunting when the crack front intersects the filler–matrix interface. Hence, crack-tip blunting seems to be the

reason for an increase in fracture toughness seen in the weakly bonded case. The same can also be deduced by comparing crack velocities between weakly and strongly bonded particles. It can be noticed from Tables 3 and 4 that both steady state and maximum velocities are consistently higher for strongly bonded particles compared to weakly bonded ones of similar particle size. Crack tip blunting retards the crack growth when crack front encounters weaker filler–matrix interface. This gives rise to lower average velocity in weakly bonded particles compared to strongly bonded ones in which crack predominantly travels through the matrix material without obstacles in the form of blunting. Crack tip blunting is also conjectured to be the cause for microcrack formation. When the crack is retarded momentarily at the blunted crack tip, additional energy is needed for re-initiation. Further, release of energy at re-initiation gives rise to microcracking. Thus, the total dissipated energy during fracture is consumed in crack propagation as well as in the formation of localized microcracks. This diversion of energy into microcrack formation is reflected in the higher fracture toughness in Tables 3 and 4. That is, fracture toughness values for weakly bonded particles are consistently higher when compared to strongly bonded ones of similar particle size.

It can be justified that for a constant filler volume fraction, decrease in particle size increases the blunting effect due to the greater number of fillers in the crack path. This suggests that fracture toughness should increase with decrease in particle size for weakly bonded particles. But this trend is not reflected in the measured fracture toughness values. It can be observed from Table 3 that in spite of the lowest steady state crack velocity, 35 μm weakly bonded particles show maximum steady state fracture toughness. Also, Fig. 9 shows an inverse relationship between crack velocity (v_{ss}) and fracture toughness (K_{Iss}) for glass-filled epoxy. This is contrary to the observation that fracture toughness increases with increase in crack velocity seen among unfilled polymeric and metallic materials. Also the fracture toughness reduces further as particle size increases or decreases relative to 35 μm particle size. This suggests that in the case of weakly bonded particles an additional mechanism is also affecting the fracture toughness. Although the data presented is limited in the case of strongly bonded fillers, 35 μm particles show slightly higher fracture toughness compared to other particle sizes. With current macroscopic observations the reasons for optimum particle size for maximum fracture toughness could not be fully explained. A complementary microscopic investigation of the fracture surfaces is essential in order to provide a more comprehensive understanding. In part II of this study, the effective mechanisms have been investigated in more detail by performing micro-measurements on the fracture surface.

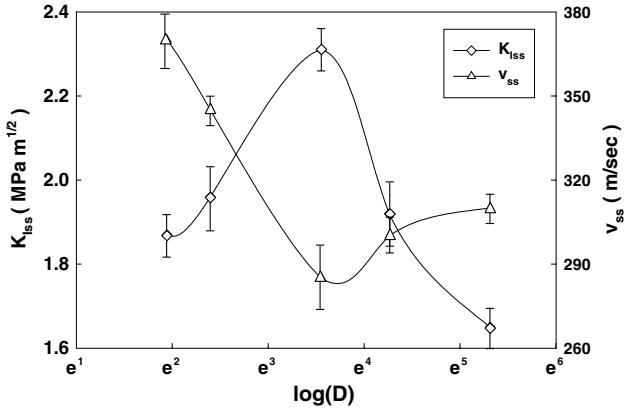

Fig. 9. Variation of steady state velocity and fracture toughness with particle size in glass-filled epoxy with weakly bonded fillers.

5. Conclusions

Preparation, characterization and crack-tip field measurements under dynamic loading conditions have been performed in glass-filled epoxy composites. Uncoated (weakly bonded) and silane coated (strongly bonded) fillers from 7 to 203 μm in mean diameter are used to prepare macroscopically homogeneous test specimens at 10% filler volume fraction. Reflection CGS and high-speed photography are used to measure crack-tip fields. Fracture parameters are evaluated using three term asymptotic field description of interferograms. Robustness and repeatability of optical measurements is demonstrated. Particle size and filler–matrix adhesion effects on fracture behavior based on the experiments can be summarized as follows:

- Neither particle size nor filler–matrix adhesion show discernible influence on elastic properties at 10% filler volume fraction.
- Both weakly and strongly bonded filler particles in the matrix show higher steady state fracture toughness (K_{Iss}) compared to unfilled epoxy.
- Significant particle size effect on fracture toughness (both initiation K_{Ii} and steady state K_{Iss} values) has been noticed in weakly bonded particles. There is a distinct optimum particle size (35 μm at 10% V_f in the current study) at which fracture toughness is at a maximum. Fracture toughness decreases as particle size increases or decreases relative to this particle size. The fracture toughness shows saturation at relatively large particle size.
- Maximum crack velocity (v_{max}) increases as particle size decreases for weakly bonded particles. Steady state velocity (v_{ss}) shows an inverse relationship with K_{Iss}. Minimum v_{ss} corresponds to the optimum particle size of 35 μm and maximum K_{Iss} in this study.

- Particle size has little or no effect on fracture toughness (K_{Ii} and K_{Iss}) in strongly bonded filler particles.
- In the case of strongly bonded filler particles, v_{max} and v_{ss} increase as particle size decreases.
- Increasing filler–matrix adhesion affects the fracture toughness negatively under dynamic loading conditions. Particle size effects are relatively more prominent in weakly bonded particles as compared to strongly bonded ones. The increase in fracture toughness (K_{Iss}) of weakly bonded particles with respect to strongly bonded ones is maximum for the optimum particle size and tends to vanish as particle size is either increased or decreased.
- Both maximum and steady state velocities v_{max} and v_{ss} increase with increasing filler–matrix adhesion strength.
- Quantitative image analysis of polished surface micrographs does not show any particle induced or coating induced agglomeration.

Acknowledgement

Authors would like to thank U.S. Army Research Office for supporting this research through grants DAAD-19-01-1-0414 and W911NF-04-1-0257 (Dr. Bruce LaMattina, Program Director). Also, enthusiastic support of Mr Chris Smith, Technical Manager of Potters Industries, Inc., is gratefully acknowledged for providing the filler materials used in this research.

References

[1] Spanoudakis J, Young RJ. Crack propagation in a glass particle-filled epoxy resin. Part 1. Effect of particle volume fraction and size. J Mater Sci 1984;19:473–86.

[2] Spanoudakis J, Young RJ. Crack propagation in a glass particle-filled epoxy resin. Part 2. Effect of particle–matrix adhesion. J Mater Sci 1984;19:487–96.

[3] Moloney AC, Kausch HH, Kaiser T, Beer HR. Review – Parameters determining the strength and toughness of particulate filled epoxide resins. J Mater Sci 1987;22:381–93.

[4] Nakamura Y, Okabe S, Iida T. Effects of particle shape, size and interfacial adhesion on the fracture strength of silica-filled epoxy resin. Polym Polym Compos 1999;7(3):177–86.

[5] Nakamura Y, Yamaguchi M. Effects of particle size on the fracture toughness of epoxy resin filled with spherical silica. Polymer 1992;33(16):3415–26.

[6] Lange FF. The interaction of a crack front with a second-phase dispersion. Phil Mag 1970;22:983–92.

[7] Evans AG. The strength of brittle materials containing second phase dispersions. Phil Mag 1972;26:1327–44.

[8] Faber KT, Evans AG. Crack deflection process. I. Theory. Acta Metall 1983;31(4):565–76.

[9] Faber KT, Evans AG. Crack deflection process. II. Experiment. Acta Metall 1983;31(4):577–84.

[10] Ahmed S, Jones FR. A review of particulate reinforcement theories for polymer composites. J Mater Sci 1990;25:4933–42.

[11] Tippur HV, Krishnaswamy S, Rosakis AJ. Optical mapping of crack tip deformations using the methods of transmission and reflection coherent gradient sensing: a study of crack tip K-dominance. Int J Fract 1991;52:91–117.

[12] Tippur HV. Coherent gradient sensing: a Fourier optics analysis and applications to fracture. App Opt 1992;31(22):4428–39.

[13] Krishnaswamy S, Tippur HV, Rosakis AJ. Measurement of transient crack-tip deformation fields using the method of coherent gradient sensing, *K*-dominance. J Mech Phys Solids 1992;40(2):339–72.

[14] Bush MB. The interaction between a crack and a particle cluster. Int J Fract 1997;88:215–32.

[15] Knight MG, Wrobel LC, Henshall JL, De Lacerda LA. A study of the interaction between a propagating crack and an uncoated/coated elastic inclusion using the BE technique. Int J Fract 2002;114:47–61.

[16] Gifkins RC. Optical Microscopy of Metals. New York: American Elsevier Publishing Company Inc; 1970. p. 168–195.

[17] Richardson JH. Optical microscopy for the materials sciences. New York: Marcel Dekker Inc; 1971. p. 592–628.

[18] Fullman RL. Measurement of particle sizes in opaque bodies. Trans AIME J Metals 1953(March):447–52.